Winkler springs for axial response of suction bucket foundations in cohesionless soil

Grecu, Sorin; Ibsen, Lars Bo; Barari, Amin

Published in:
Soils and Foundations

DOI (link to publication from Publisher):
10.1016/j.sandf.2020.10.010

Publication date:
2021

Document Version
Publisher's PDF, also known as Version of record

HOSTED BY

ELSEVIER

Available online at www.sciencedirect.com

ScienceDirect

Soils and Foundations 61 (2021) 64–79

www.elsevier.com/locate/sandf

Technical Paper

Winkler springs for axial response of suction bucket foundations in cohesionless soil

Sorin Grecu *, Lars Bo Ibsen, Amin Barari

Department of the Built Environment, Aalborg University, Thomas Manns Vej 23, 9220 Aalborg Ø, Denmark

Received 30 January 2020; received in revised form 5 October 2020; accepted 6 October 2020
Available online 13 December 2020

Abstract

Jacket structures mounted on suction buckets carry potential as cost-efficient foundations for next-generation 10 MW+ offshore wind turbines located in transitional water depths. Given this foundation method, resistance to overturning moment relies mainly on the axial response of the buckets. In practice, suction bucket foundations can be modelled as "Beams on Non-Linear Winkler Foundation" where soil is idealised as non-linear springs. This paper describes the derivation process of static load-transfer or t–z curves for suction buckets installed in cohesionless soil. The mathematical formulation of the curves is based on regression analysis of data obtained from 100 axisymmetric numerical models in a medium characterised by the Hardening Soil model for representing the stress–strain relationships for Frederikshavn sand, which is a typical offshore sand. Various bucket dimensions, soil properties and drainage conditions were simulated considering tension and compression, in order to describe frictional behaviour at the skirt–soil interface. The non-linear springs' properties are therefore linked to foundation diameter, friction angle and vertical overburden pressure. By superimposing the effects of all springs, load–displacement curves are generated and compared with results from available experimental and numerical studies on suction buckets, revealing reasonable agreement. It is shown that the existing t–z formulations for piles are inapplicable to large-diameter suction buckets.

Keywords: Friction; Numerical modelling; Load–displacement curves; Suction bucket; Soil/structure interaction

1. Introduction

Recent trends within the offshore wind industry reveal that an increasing number of offshore wind farms are being erected further from coastlines (Wang et al., 2018). Normally, larger distances are associated with deeper waters and higher environmental loads (Larsen et al., 2013; Ibsen et al., 2014). At the same time, high capacity 10 MW+ offshore wind turbines (OWTs) are becoming more common. These factors pose questions in terms of foundation solutions for such structures.

Monopiles represent the industry standard and their performance in shallow waters up to 30–40 m deep is unquestionable. However, this solution might become impractical in larger water depths. One of the reasons is that it might not be possible for manufacturers to produce monopiles that would fulfil tougher design requirements. In light of this fact, alternative viable options comprise an active research area. One of these options is the suction bucket jacket (SBJ).

SBJs represent a promising foundation concept for OWTs in transitional water depths of 30–60 m (Oh et al., 2018). These are lattice structures, typically with three or four legs, that are supported by suction buckets. Within the oil & gas sector, suction buckets are widely used for anchoring floating platforms (Tjelta, 2015). Unfortunately,

Peer review under responsibility of The Japanese Geotechnical Society.
* Corresponding author.
E-mail address: sgre@build.aau.dk (S. Grecu).

https://doi.org/10.1016/j.sandf.2020.10.010
0038-0806/

the associated design practices cannot be directly translated for SBJs. In contrast to heavy oil/gas platforms, OWTs are relatively light, therefore horizontal environmental loads are most likely to become a driving design aspect.

Fig. 1(a) illustrates the load transfer mechanism in a typical jacket structure. Environmental loads generate an overturning moment that triggers a "push–pull" mechanism whereby individual buckets are axially loaded either in tension or compression. Although uplift would occur at rare occasions, such as extreme storm events, it is still a critical design issue. Thus, overall stability is closely connected to axial response of suction buckets. In this paper, focus is placed on friction between bucket skirt and adjacent soil during vertical monotonic loading (see Fig. 1(b) and Fig. 1(c)).

A commonly adopted method for modelling soil–structure interaction is the Winkler approach (Winkler, 1867). Its principle lies in idealisation of the structure into discrete elements, where each of them is attached to a non-linear spring that simulates soil reaction at any given vertical deflection of its associated element (see Fig. 2). The behaviour of each spring is described by a relationship between shear stress in the soil medium in immediate proximity to the structure, τ, and relative soil–structure vertical displacement, z. The graphical representation of this relationship is referred to as "t–z curve" or "load-transfer curve".

Load-transfer curves comprise a convenient means to assess axial behaviour of piles. In fact, all existing t–z formulations relate strictly to deep slender substructures. The majority of proposed relationships were derived empirically from test data or analytically from theoretical considerations (Seed & Reese, 1957; Coyle & Sulaiman, 1967; Vijayvergiya, 1977; Randolph & Wroth, 1978; Kraft et al., 1981; Fleming, 1992; Wang et al., 2012; Nanda & Patra, 2014; Bohn et al., 2016; Zhou et al., 2019). The success of the Winkler method is explained by its capability to account for soil's inherent non-linearity and for random layer distribution while exhibiting relative mathematical ease (Lombardi et al., 2017).

The motivation for the current study stems from the idea that existing t–z curves are prone to misrepresenting the frictional response of suction buckets subjected to axial loading. The diameters of piles used for calibrating these curves generally do not exceed 2 m (Bohn et al., 2016), while the expected diameters of suction buckets range from 10 m to 20 m. The unreliability of applying pile-specific curves to buckets is rooted in notable differences between behaviours of the two foundation types. Suction buckets have relatively small length-to-diameter ratios and embedment depths, and thus their associated failure mechanisms exhibit features related to shallow footings and to piles. Moreover, internal mechanisms develop within entrapped soil and their effects on internal skirt friction cannot be ignored. For example, following failure, an inverted scoop mechanism arises due to the existence of deformable ground within the skirts. This phenomenon is discussed in Barari & Ibsen (2012).

This paper proposes a novel set of t–z curves for suction buckets installed in cohesionless soil based on numerical modelling. The set comprises four distinct formulations defined according to cases that combine drainage conditions (drained and undrained) and loading scenarios (tension and compression). Firstly, distinct drainage conditions require consideration, since excess pore water pressure affects soil–structure interaction through its influence on the effective stress field. In their numerical studies,

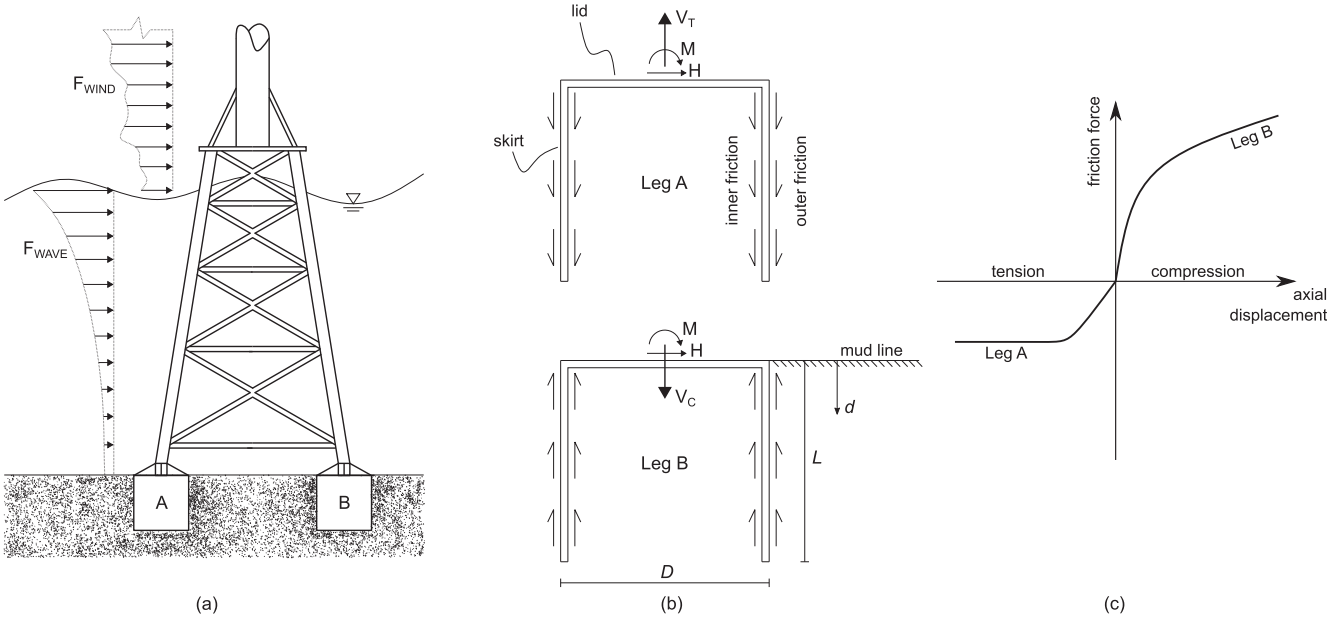

Fig. 1. (a) Schematic elevation of a four-legged jacket structure resting on suction buckets; (b) Skin friction contributes to the stability of the system by counteracting the imposed vertical loads. Other stabilising factors are purposely omitted in the sketch; (c) The loading direction plays a major role in the frictional behaviour of suction buckets.

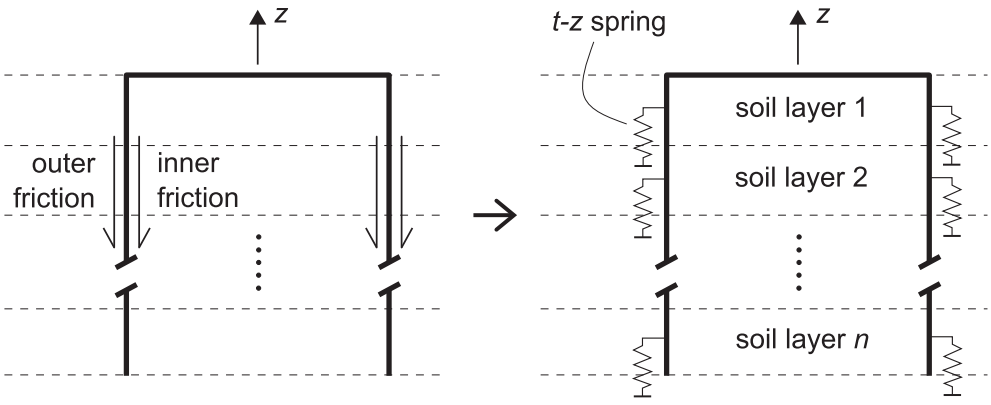

Fig. 2. Idealisation of the system whereby soil–structure interaction is represented by axial springs.

Thieken et al. (2014) and Shen et al. (2017) showed that external skirt friction tends to increase with displacement rate during uplift, while the internal one follows an inverse trend. Secondly, the loading direction determines the failure mechanism, as described by Mana et al. (2012) in their discussion of centrifuge test results, which in turn reflects upon the development of skirt friction. This justifies the necessity of formulating t–z curves for each loading direction separately.

The advantage of the proposed load-transfer curves lies in their straightforward formulation in terms of bucket diameter, D, initial effective vertical overburden pressure, σ'_{v0}, and friction angle, ϕ, of sand. The last two variables are basic geotechnical parameters that can be obtained from conventional tests. Within the Limit State Design approach, the non-linear axial springs play a significant role in Ultimate Limit State (ULS) checks. The contribution of skirt friction to the vertical capacity of the foundation may be estimated by constructing load–displacement relationships based on t–z curves and identifying the threshold associated with a given criterion. In case of drained uplift, the sum of skirt friction and self-weight is equivalent to the total axial capacity. It is acknowledged that in cases of compressive and undrained tensile loading there is significant contribution to the total vertical resistance resulting from soil reaction under the bucket lid/skirt toe and differential water pressure, respectively. The paper omits the study of these topics and focuses solely on skirt friction.

Since only monotonic loading is considered in the present study, the derived t–z curves are static, i.e. they do not incorporate the effects of cyclic and dynamic loading. Nonetheless, the proposed load-transfer relationships can be implemented in the analysis of target natural frequency of the system. This is an essential aspect of OWT design, as these structures are continuously subjected to harmonic excitation.

The new t–z formulations are verified by comparison with results from relevant experimental and numerical studies, and with pile-specific relationships given by design codes.

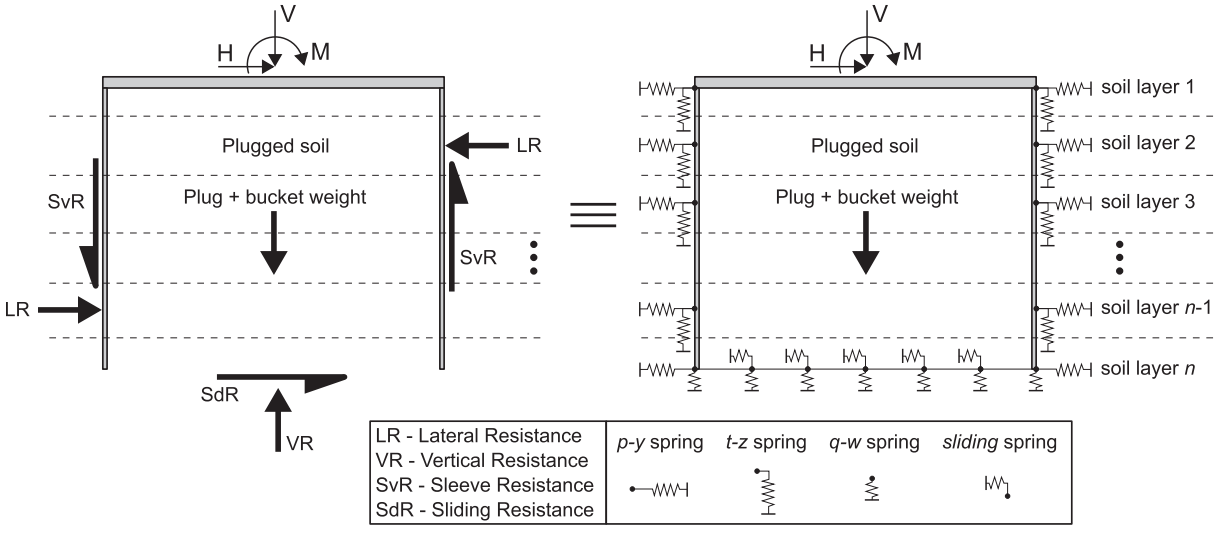

Fig. 3. The four types of springs for the analysis of suction buckets. Reproduced from Vahdatirad et al. (2016).

2. The physics of the problem and a Winkler model

Vahdatirad et al. (2016) modelled a suction bucket in sand by an analytical method — the Winkler method, where springs along the skirt and bottom were assigned as shown in Fig. 3 to estimate soil pressure in various directions: horizontal springs (p–y) and vertical springs (t–z for skirt response and q–w for tip resistance). The model, referred to as "multi-spring Winkler model", uses a p–y formulation suggested by Østergaard et al. (2015) and an efficient numerical routine to solve the system equations. The t–z curves provided by API (2000) were taken into account.

API (2000) assumes a linear t–z curve for cohesionless soil deposits, followed by no strain softening under monotonic loading. This conservative approach supposes that ultimate capacity is reached at the settlement of 0.00254 m and follows the general understanding that resistance does not increase further with additional settlement.

In literature one may find hyperbolic or parabolic shapes of stress–strain relationships to predict soil behaviour, e.g. the hyperbolic model proposed by Kraft et al. (1981). However, the existing expressions cannot be directly applied to large-diameter suction buckets to predict non-linear soil behaviour, let alone other interface non-linearities such as separation (gapping) and uplifting that may take place under a strong static event. Many of these formulations do not consider inner friction or excess pore water pressure gradients, both of which play major roles in the behaviour of bucket foundations. Moreover, the expressions were typically validated with very small-diameter test piles (<0.5 m). In an effort to bridge this apparent gap in the available methodologies for analysis of axially loaded suction buckets relevant for jacket structures, this paper develops a Winkler-type model described by four types of axial springs, each marked by its own formulation. The aim is to present a sound engineering solution underlined by a methodology that has the following attributes:

- It provides the response to static uplift/compression loading applied at the top of a bucket.
- It handles the drained and undrained soil conditions.
- It takes both soil inelasticity and geometric (interface) non-linearities into account in a realistic fashion.

3. Numerical modelling

Research involving numerical simulations of suction bucket foundations by means of finite-element (FE) method illustrates the technique's efficacy and convenience for assessing the behaviour of the system (Barari & Ibsen, 2012, 2018; Achmus et al., 2013; Achmus & Thieken, 2014; Mana et al., 2014; Thieken et al., 2014; Østergaard et al., 2015; Achmus & Gütz, 2016; Park et al., 2016; Park & Park, 2017; Sørensen et al., 2016; Shen et al., 2017; Lu & Luo, 2018). On grounds of conceptually identical purposes, this paper along with two studies conducted by researchers at Aalborg University, Østergaard et al. (2015) and Vahdatirad et al. (2016), develops a Winkler-type model that comprises a set of four axial springs.

Proper assessment of foundation capacity requires assessment of the influence of drainage conditions. If site or loading conditions are such that dissipation of pore pressure is either prevented or delayed within the period of interest, then an undrained bearing capacity analysis would be predominant. Increasing the intensity of loading in a very short period (i.e. storm event) generates larger excess pore pressures in granular material which in turn implies that the sand deposit exhibits larger resistance to pore water pressure dissipation both horizontally and vertically (Barari et al., 2017).

Large-diameter offshore foundations such as buckets reduce the ability of excess pore pressures to dissipate rapidly from underneath turbine structures by increasing drainage path (if all else remains constant). This longer drainage path may result in larger and more sustained net excess pore pressures under wider OWTs.

The conducted analyses are based on a two phase (solid–fluid) coupled finite-element formulation of Chan (1988) and Zienkiewicz et al. (1990), based on the Biot theory of porous material (Biot, 1962). The quasi-static u–p formulation included soil deformation, u, and pore pressure, p, that were treated simultaneously by means of a coupled analysis.

Single buckets subjected to axial loading and installed in uniform sand were modelled. The computation time was significantly reduced by taking advantage of the system's cylindrical symmetry. It is worth noting that the adopted approach excludes the possibility of accounting for group effects present in multi-footed foundations. The magnitude and consequences of these effects for suction bucket jackets depend on factors such as bucket dimensions, footprint size, loading and ground conditions, as explained in Sturm (2017), and related studies may be based on global FE models involving all jacket legs.

A total of 100 axisymmetric finite-element models were constructed with Plaxis 2D (Plaxis, 2017). Each model comprised a combination of various input parameters, which are described in the following list.

- Bucket dimensions: lid diameter, D, and skirt length, L. The aspect ratio was equal to unity in all models. Keeping in mind the potential size of suction buckets supporting jacket structures, the following values for D and L were used: 10, 13, 15, 18 and 20 m.
- The peak angle of internal friction, ϕ, was implemented as an independent variable dictating the properties of Frederikshavn sand, i.e. all soil parameters were defined as functions of ϕ. The process of establishing these functions is explained later in the paper. Five friction angles

were considered: 30°, 33°, 35°, 38° and 40°. Alternatively, the relative density, D_r, may be viewed as the independent variable instead of ϕ, since they are directly correlated through Eq. (1).

- The vertical displacement rate of the bucket, v, was given values of 1 and 10 mm/s to simulate drained and undrained conditions, respectively. These velocities are appropriate for achieving both drainage extremes, as revealed by comparisons with outputs from models that consider fully drained and undrained conditions. This issue is further addressed in Section 3.2.1. All models employ a time-dependent coupled formulation to analyse simultaneous development of soil deformations and excess pore water pressure.
- Displacement direction was defined as either monotonic upwards (tensile loading) or downwards movement (compressive loading).

Fig. 4 illustrates the mesh composed of triangular fifteen-node quartic elements and the domain extents relative to bucket dimensions. The mesh around the bucket was refined in order to obtain a clear picture of stress distribution in the region of interest, where gradients are largest. A convergence study gave the optimal degree of local h-refinement. The procedure involved examining soil–structure interface shear stress changes with respect to a gradually increasing number of elements. Concurrently, a domain size analysis ensured that the model edge effects became negligible, in the context of simulating realistic site conditions. This analysis consisted of expanding the domain vertically and horizontally (d and r in Fig. 4) until the shear stresses along the boundaries became almost zero, which indicated a fully developed failure mechanism.

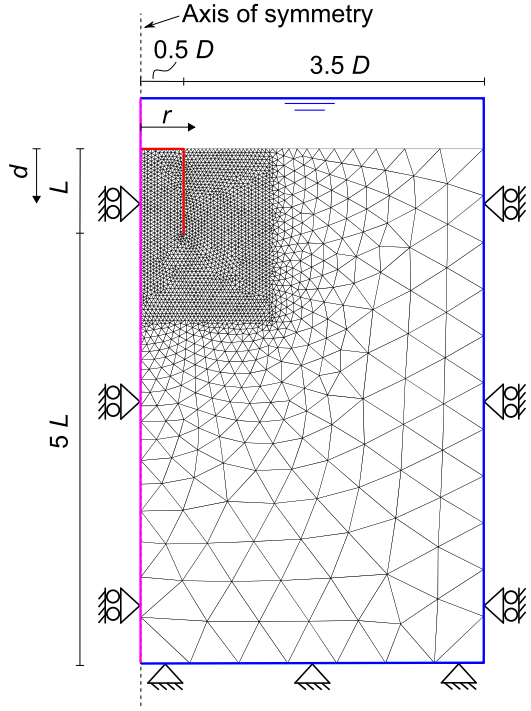

Fig. 4. FE model set-up: bucket (red), impermeable hydraulic boundary (purple), fully permeable hydraulic boundary (blue).

The nodes along the axis of symmetry and along the opposite edge were horizontally restrained, while the bottom edge was fully fixed. Seepage was allowed through all model boundaries. As an intrinsic property of axisymmetric models, no flow was possible through the axis of symmetry. Vertical displacements were prescribed to all nodes in elements that defined the bucket, whilst restricting horizontal deflections thereof. It is stressed that prescribed displacements were assigned to the embedded part of the foundation as well, under the assumption of a structure exhibiting rigid body behaviour.

The numerical analyses followed the following steps to simulate actual field conditions:

(1) *K0* procedure: soil initially undergoes geostatic stresses.
(2) Foundation and interface elements: a part of soil is replaced by the foundation. The bucket analysis does not address the construction process, which means the foundation is "wished-in-place". In practice, the soil softening phenomenon associated with the installation process is unavoidable, but it can be accounted for by modifying the soil strength and stiffness parameters accordingly (Hossain & Randolph, 2009). Nevertheless, Achmus et al. (2013) and Zafeirakos & Gerolymos (2016) assumed that installation effect is of minor importance regarding the general bucket performance and its degrading influence was therefore disregarded in their analyses.
(3) Nil-step phase: displacements and small strains due to activation of the structure are reset to zero.
(4) Loading phase: prescribed displacements are applied to the bucket.

3.1. Material modelling and properties

The Hardening Soil model (Schanz et al., 1999) with small-strain stiffness (HSsmall) defined the constitutive relationships for cohesionless soil, with input parameter values related to Frederikshavn sand at various compaction states.

Firstly, the link between relative density, D_r, and friction angle, ϕ, is established by rearrangement of empirical relationships derived by Bolton (1986), and is expressed by

$$D_r = \frac{\phi - \phi_{crit} + 3R + \Delta\phi_1}{3\left(Q_{min} - \ln\frac{p'}{1kPa}\right) - 3} \quad (1)$$

where $\phi_{crit} = 33°$ is the critical friction angle; $\Delta\phi_1 = 2°$ is the correction corresponding to 5–10% of silt content; $Q_{min} = 10$ is a coefficient related to quartz sands; $p' = 100$ kPa is the reference effective mean stress; and $R = 1$ is a fitting coefficient. The initial void ratio, e, can be com-

puted by using the definition of D_r. According to Nielsen et al. (2012), the minimum e_{min} and maximum e_{max} void ratios of Frederikshavn sand are equal to 0.64 and 1.05, respectively.

Based on Janbu's tangent modulus concept (Janbu, 1967), outlined in DNV (1992), the reference oedometer modulus, E_{oed}^{ref}, is formulated in terms of D_r as follows

$$E_{oed}^{ref} = 16,142D_r^2 + 19,987D_r + 3688(\text{in kPa}) \quad (2)$$

where the superscript denotes the modulus at a reference confining stress of 100 kPa. The coefficients in Eq. (2) are found by means of regression analysis of data related to Norwegian inorganic sands, presented in DNV (1992).

Adhering to theory of elasticity, it is roughly assumed that the reference secant modulus, E_{50}^{ref}, depends on E_{oed}^{ref} in the following manner (Østergaard et al., 2015)

$$E_{50}^{ref} = \frac{1 - \nu - 2\nu^2}{1 - \nu} E_{oed}^{ref} \quad (3)$$

which implies equivalence between E_{50}^{ref} and Young's modulus, E. Poisson's ratio, ν, can be computed according to

$$\nu = \frac{1 - \sin\phi}{2 - \sin\phi} \quad (4)$$

The reference unload/reload modulus is estimated as $E_{ur}^{ref} = 3E_{50}^{ref}$. The dependency of soil stiffness on confining stress is accounted for in the Hardening Soil model, as described by Schanz et al. (1999). For the sake of brevity, the relationships between reference moduli, which act as input parameters, and calculated stress-dependent moduli are not presented in this paper.

Two additional parameters are required to model small-strain stiffness: reference shear modulus at very small strains ($\varepsilon < 10^{-6}$), G_0^{ref}, and threshold shear strain, $\gamma_{0.7}$, at which the reference secant shear modulus $G_s^{ref} = 0.722G_0^{ref}$. According to Hardin & Black (1969), the former may be estimated as

$$G_0^{ref} = 3300\frac{(2.97 - e)^2}{1 + e}\sqrt{p^{ref}} \quad (5)$$

where the reference effective mean stress $p^{ref} = 100$ kPa. The threshold shear strain, $\gamma_{0.7}$, is computed as follows

$$\gamma_{0.7} = \frac{2c'(1 + \cos 2\phi) - \sigma_v'(1 + K_0)\sin 2\phi}{9G_0^{ref}} \quad (6)$$

where effective cohesion $c' = 0.1$ kPa; earth pressure coefficient at rest $K_0 = 1 - \sin\phi$; and σ_v' is the effective vertical stress. Eq. (6) is derived from the definition of reference shear strain (Hardin & Drnevich, 1972) and by expressing the shear strength in the context of Mohr-Coulomb failure criterion. In absence of relevant laboratory test data, this formulation proves convenient since an estimation of $\gamma_{0.7}$ is obtained for each soil state, see Table 1.

Sjelmo (2012) conducted a series of permeability tests on Frederikshavn sand. After calibrating the test results for a water temperature of 9 °C, the hydraulic conductivity, k, is expressed in terms of void ratio as shown in Eq. (7).

$$k = 0.4e^2 + 0.2e + 0.03(\text{in mm/s}) \quad (7)$$

The interface friction angle, δ, is assumed as 2/3 of ϕ, adopting indicative values specified by API (2000) and following other numerical studies (Achmus et al., 2009, 2013; Park et al., 2016).

Table 1 summarises all five sets of soil parameters used for numerical modelling, where each set corresponds to a chosen friction angle.

Table 1
Soil parameters used in the FE models.

Parameter: unit	Set 1	Set 2	Set 3	Set 4	Set 5
ϕ: degrees	30	33	35	38	40
D_r: %	15.2	37.9	53.1	75.8	91.0
e	0.99	0.89	0.83	0.74	0.68
ψ: degrees	0	0	2	5	7
γ_{sat}: kN/m^3	18.3	18.7	19.0	19.4	19.8
γ_{dry}: kN/m^3	13.3	13.9	14.4	15.2	15.7
E_{50}^{ref}: kPa	4727	9717	14,044	22,129	28,622
E_{oed}^{ref}: kPa	7091	13,589	18,849	28,133	35,251
E_{ur}^{ref}: kPa	14,182	29,150	42,131	66,387	85,867
m	0.5	0.5	0.5	0.5	0.5
G_0^{ref}: kPa	65,228	75,034	82,300	94,449	103,490
$\gamma_{0.7}$: 10^{-3} m/m	0.2218	0.1973	0.1813	0.1583	0.1438
ν	0.33	0.31	0.30	0.28	0.26
K_0	0.5	0.46	0.43	0.38	0.36
δ: degrees	20	22	23.3	25.3	26.6
k: 10^{-5} m/s	20.843	15.946	13.053	9.274	7.128

Rigid body properties were attributed to the modelled bucket, in order to reduce the influence of structural deformations on soil response. This assumption was enforced in two steps: (*a*) by prescribing displacements to all structural elements, including those that model the bucket skirt; (*b*) by deliberately setting a large elastic modulus of steel, thereby increasing the bending and axial stiffness of the structure. It is worth noting that in general the flexibility of the structure influences the foundation stiffness (Skau et al., 2019).

The unit weight of water, γ_w, was set to 10 kN/m^3 and the gravitational acceleration to 9.81 m/s^2.

3.2. Qualitative description of FE results

In this section, results obtained from the numerical analyses are presented and discussed. The model with parameters $D = L = 15$ m and $\phi = 35°$ serves an illustrative purpose throughout the entire paper.

3.2.1. Failure mechanisms

Typical load transfer mechanisms of buckets under tensile loads are shown in Fig. 5. A vertical sliding failure is dominant in case of full drainage (Fig. 5(a)). It normally occurs when the bucket's lid is not sealed or the foundation is subjected to long-term tensile loading.

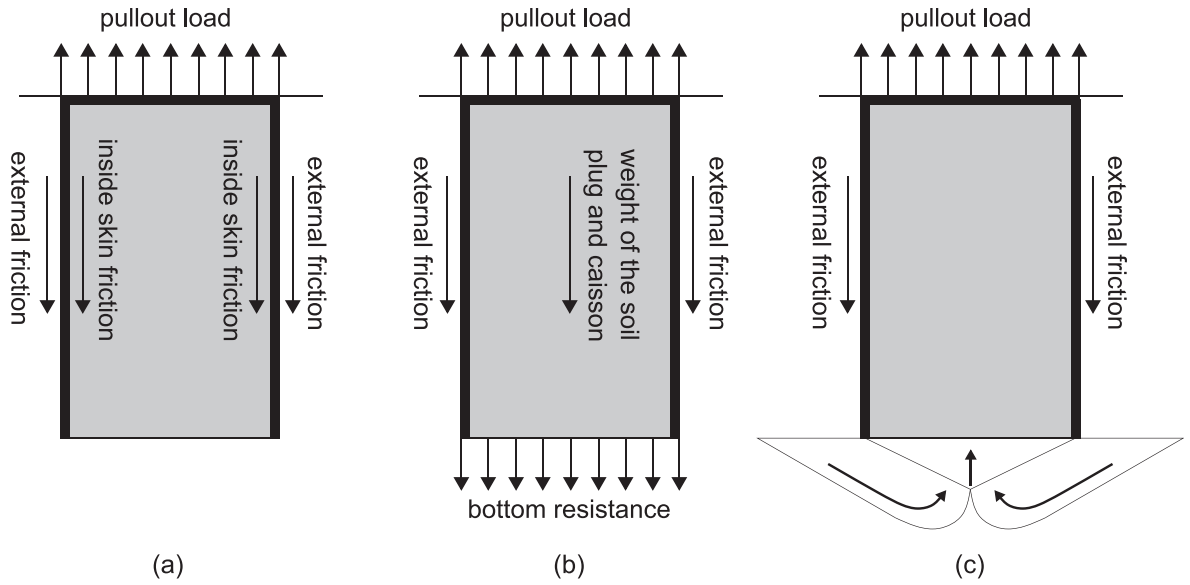

Fig. 5. Failure mechanisms for suction buckets under tensile loading: (a) sliding; (b) bottom resistance; (c) reverse bearing capacity. Adapted from Deng & Carter (2002).

Fig. 5(b) explains the response when partial drainage occurs and passive suction effect is limited owing to pore pressure dissipation. The mechanism that corresponds to "bottom resistance failure" consists of outside skin friction, weight of the soil plug and passive suction at the bottom of the bucket which contribute to the total vertical resistance. This failure mode is of particular importance when the soil–foundation system is subjected to intermediate or short term tensile loading. The mechanism in Fig. 5(c) involves "reverse bearing capacity failure" that occurs when the foundation is subjected to short term tensile loading along with the assumption of globally undrained conditions over the entire loading period. The contribution of outside skin friction is similar to the former failure mode, unless a fraction of tensile loading is governed by reverse bearing capacity.

Fig. 6(a) and 6(b) show the FE results for $L/D = 1$ which adequately capture the kinematic failure mechanisms under various drainage and loading conditions. Following previous observations, soil plugs form during undrained uplift and compression. In the latter case, the underlying mechanism appears proportionally deeper than the one associated with uplift. Similar trends were reported by Mana et al. (2012) based on centrifuge tests.

During drained tensile loading, only minor soil displacements take place and the bucket lid separates from the soil surface. This is indicative of nearly frictional behaviour. For drained compression, the inner soil mass does not move together with the bucket as a plug, and the vertical soil displacements within the bucket decrease with depth and with distance to centreline.

The excess pore water pressure plots in Fig. 6(c) and (d) reveal insignificant pressure developments when the bucket is displaced at a rate of 1 mm/s, meaning that drained conditions are simulated appropriately. As an additional check, the total vertical response of the bucket obtained by means of a coupled consolidation formulation is compared with the one based on fully drained conditions (no excess pore water pressure generation). The comparison study concludes on nearly identical results between the two types of analyses.

Considering the displacement rate of 10 mm/s, the coupled formulation in Plaxis performs better than the perfectly undrained analysis in that it describes the mechanics of the system more accurately. It can successfully compute soil plugging and thus it falls closer to the theoretical extreme of undrained condition. Vaitkunaite et al. (2016) achieved nearly undrained behaviour through physical model testing in a pressure tank. The results of this experimental study appear consistent with the coupled formulation.

It is worth noting that the lower bound for pore water pressure is set by the cavitation pressure, u_{cav}, which is about −100 kPa (tension is negative) and relates to the atmospheric pressure. This is relevant for undrained tensile loading, where negative excess pore pressure is expected to arise. The amount of allowable excess pore pressure, Δu_{max} depends on the hydrostatic pressure at a given depth, u_{hyd}, and can be estimated as $\Delta u_{max} = -u_{cav} + u_{hyd} = -u_{cav} + \gamma_w h_w$, where h_w is the height of the water column. The FE models involved water depths large enough so that pore water pressure does not reach the cavitation limit.

3.2.2. Development of t–z curves

Within the analysis of soil–structure friction, the extracted data relates to shear stress extracted from interface elements, rather than from soil elements adjacent to the structure. This modelling framework follows a comparison study which confirmed that larger stresses occur in interfaces (Wolf et al., 2013). The interface stress points

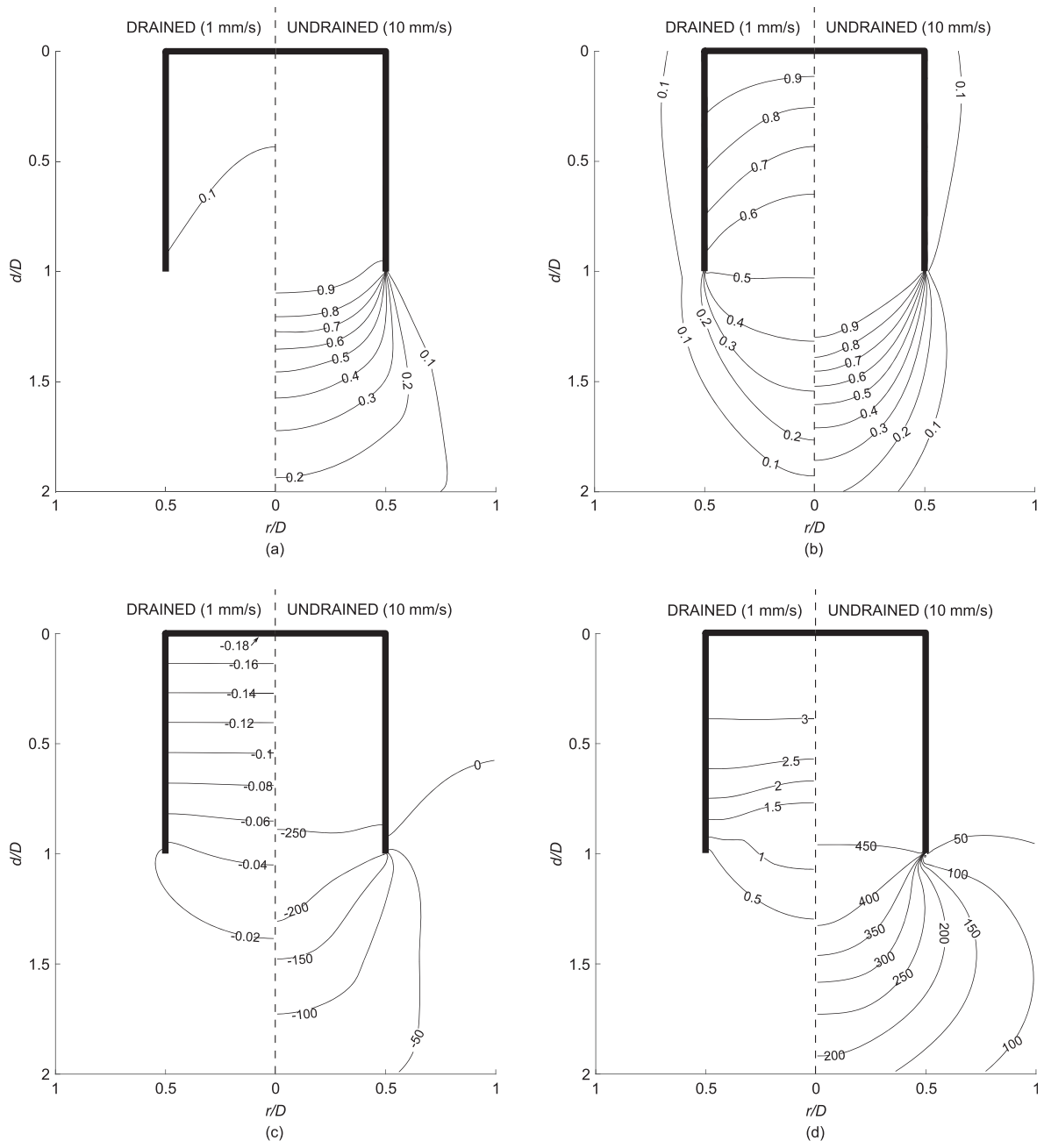

Fig. 6. Normalised vertical displacement field at the last loading stage: (a) tensile loading; (b) compressive loading. Excess pore water pressure field (tension = negative) at the last loading stage: (c) tensile loading; (d) compressive loading.

are grouped into segments (hereafter referred to as "layers") of equal lengths. The stress values generated from points within a layer are averaged for every calculation step. A layer thickness of ca. 0.8 m proves to be optimal with regards to encompassing enough stress points while maintaining a refined depiction of the shear stress gradient.

Fig. 7 and Fig. 8 show plots of layer-averaged interface shear stress against vertical displacement of the structure in case of tensile and compressive loading, respectively. Each curve is linked to a mid-layer depth. It should be noted that these figures show only 5 layers to highlight how shear stresses develop at different points along the skirt. The curves related to uppermost and lowest layers diverge significantly from the rest and exhibit larger non-linearities. Therefore, they are treated as outliers and are excluded from the forthcoming statistical analysis. The errors stemming from this approach are of a minor degree, as presented later in the paper.

The bilinear curves depicted in Fig. 7(a) are identical with the ones recommended by API (2000) in that stress increases linearly until a peak value, τ_p, is reached ("pre-failure" part), after which it becomes constant ("post-failure" part). In drained conditions, the upwards movement of the bucket leads to skin friction along inner and

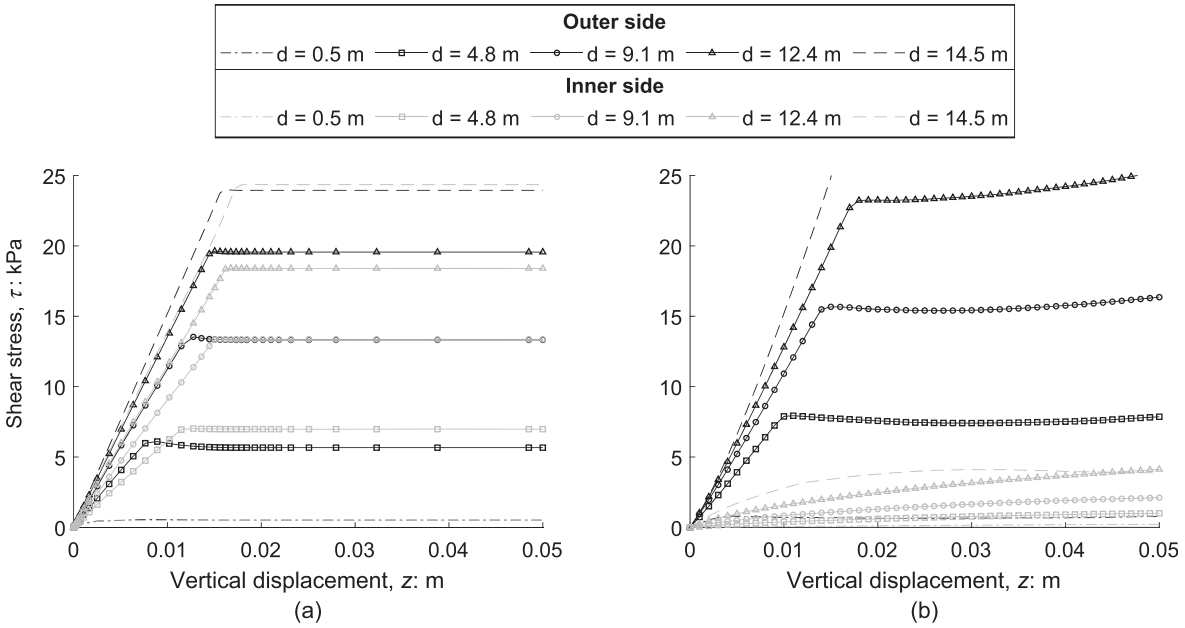

Fig. 7. Shear stress development in the soil-structure interface at various depths below mudline, d, during tensile loading: (a) drained conditions; (b) undrained conditions.

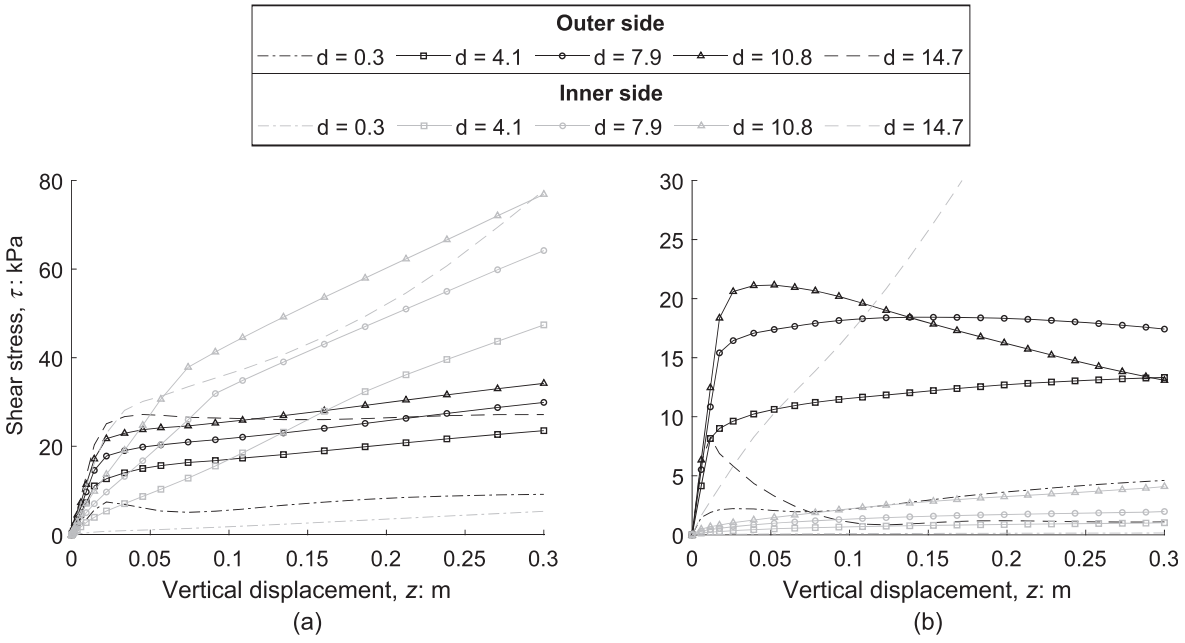

Fig. 8. Shear stress development in the soil-structure interface at various depths below mudline, d, during compressive loading: (a) drained conditions; (b) undrained conditions.

outer side of the skirt face developing in similar manners and contributing almost equally to axial resistance. The vertical displacement at which the peak stress occurs, z_p, increases non-linearly with depth. At the same time, such dependency is observed in terms of stiffness.

In presence of groundwater flow, significant differences arise between inner and outer friction (see Fig. 7(b)). Inside the bucket, the upward flow reduces the vertical overburden stress, which in turn decreases the maximum possible skin friction. This effect becomes stronger towards the skirt tip, where the hydraulic gradient is higher. Simultaneously, the confined soil mass movement in tandem with the bucket means small relative soil–structure displacements. These two factors lead to relatively low shear stress values and almost constant stiffness. Conversely, the downward groundwater flow on the outer side increases the effective weight of soil, thus shear stress attains larger values in comparison with the opposite side. Moreover, the ultimate

shear stress, τ_u, does not correspond with a certain peak, since the post-failure curves exhibit an increasing trend, in contrast to drained tensile loading.

Regarding drained compressive loading, Fig. 8(a) reveals continuous stress growth without clear peaks along inner skirt. This behaviour results from the bucket lid that acts as a surcharge on the entrapped soil mass, thereby gradually increasing the effective normal stress on the inner skirt area. The initial outer response resembles the one observed in case of drained tensile loading (cf. Fig. 7(a)), however the post-failure part is marked by linearly increasing stress. It is apparent from Fig. 8(b) that inner skirt friction is independent of loading direction in context of undrained conditions (cf. Fig. 7(b)). The effects of relatively fast groundwater flow around the skirt toe are reflected by the curves linked to skirt extremities.

4. Formulation of *t–z* curves for tensile loading

Observing the curves presented in Fig. 7, three conclusions may be drawn with regards to formulating a mathematical model of axial spring stiffness for buckets subjected to tension.

- It might prove convenient to study the total frictional response by superimposing the curves related to inner and outer skirt faces. Since the two responses are almost identical in the drained case scenario, the total effect is only expressed by a change in magnitude, while the curves' shapes are preserved. For undrained conditions, outer skirt friction constitutes the major part of the total response (~80%), which means that the corresponding curves are altered to an insignificant degree upon including the effect of inner skirt friction.
- A piecewise function can be employed to represent bilinear curves, with its condition being established in connection with vertical displacements at which the peak shear stresses occur, z_p.
- Normalisation with respect to τ_p and z_p can be applied so that all peaks are located at (1,1) in the τ/τ_p–z/z_p plane. The result is the complete alignment of curves related to all models. In this context, it becomes clear that the core goal is establishing general expressions for τ_p and z_p. For practicality, the expressions may include relevant readily-available parameters as variables, namely bucket diameter, D, effective vertical stress, σ'_v, and friction angle, ϕ.

4.1. Drained conditions

The *t–z* curve for representing the drained tensile response of suction buckets in sand is illustrated in Fig. 9 and its associated function is given by Eq. (8). In Fig. 9, the λ-parameter defines the rate of increase in shear stress during post-failure.

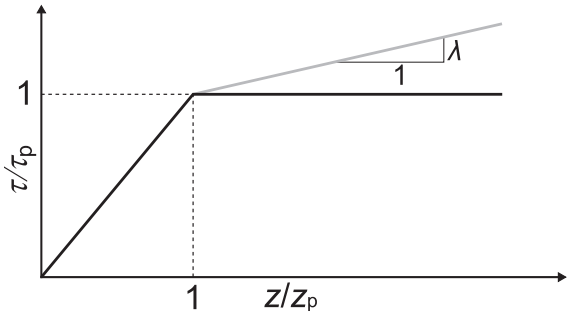

Fig. 9. Schematic t-z curves proposed for assessing the frictional response of suction buckets under tensile loading in cohesionless soils given drained (in black) and undrained (in grey) conditions. The curves overlap in the pre-failure part.

$$\frac{\tau}{\tau_p} = \begin{cases} \frac{z}{z_p} & \text{for } \frac{z}{z_p} < 1 \\ 1 & \text{for } \frac{z}{z_p} \geq 1 \end{cases} \tag{8}$$

4.1.1. Peak shear stress, τ_p, and peak displacement, z_p

Regression analysis using data from the 25 numerical models that involve drained tension is performed in order to assess the dependency of τ_p and z_p on bucket geometry, sand strength and vertical overburden pressure. Examining Fig. 10, it is seen that a power law of the form $f(x) = Ax^B$ constitutes an appropriate function for fitting data regarding each model individually. The outcoming R^2-values fall within ranges of 0.99–1.00 and 0.65–0.98 in connection with fitting of τ_p and z_p, respectively. A number of 25 values for unitless parameters A and B are obtained, which allows the investigation of A and B as functions of bucket diameter and friction angle. The expressions for τ_p and z_p can be written as

$$\frac{\tau_p}{\sigma_a} = A_\tau \left(\frac{\gamma' d^2}{\sigma_a D \tan\phi} \right)^{B_\tau} \tag{9}$$

$$\frac{z_p}{D_{ref}} = A_z \left(\frac{\gamma' d^2}{\sigma_a D \tan\phi} \right)^{B_z} \tag{10}$$

where the subscripts denote the link to the corresponding dependent variable; $\sigma_a = 100$ kPa is the atmospheric pressure and $D_{ref} = 15$ m is the reference bucket diameter.

4.1.2. Parameters a and b

The coefficients A_τ, A_z, B_τ and B_z are treated separately in a multivariable analysis to describe their relation to D and ϕ. To achieve unitless quantities, the former is normalized with respect to $D_{ref} = 15$ m, while the friction angle is represented through its tangent. Bivariate first- or second-order polynomials are used for surface fitting. Table 2 displays the results of the parametric study.

An exception is made for B_τ, since it exhibits weak correlation with either D or ϕ and its values are bound between 0.5601 and 0.5717. Using the average $B_\tau = 0.5685$ proves to introduce negligible error between

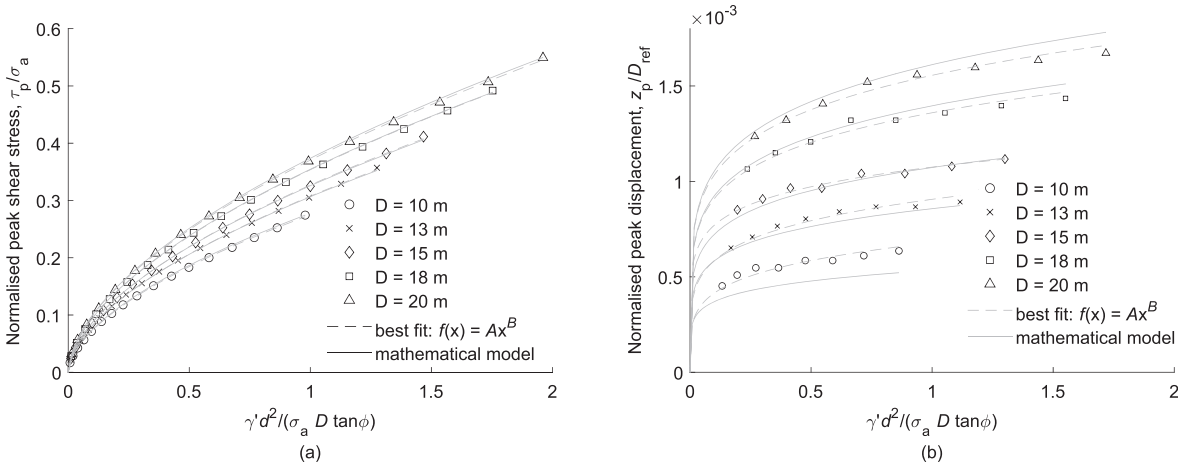

Fig. 10. Curve fitting of data from five models involving various bucket diameters and identical soil properties (marked by $\phi = 35°$) and estimations based on the established mathematical models: (a) peak shear stress; (b) displacements at which the peak shear stresses occur.

Table 2
Summary of β-coefficients used for modelling the drained tensile response. Here $x = D/D_{ref}$ and $y = \tan\phi$.

Parameter	Fitting function	β_1	β_2	β_3	β_4	β_5	R^2
A_τ	$f(x,y) = \beta_1 + \beta_2 x + \beta_3 y$	−0.066	0.145	0.351	–	–	0.9920
A_z	$f(x,y) = \beta_1 + \beta_2 x + \beta_3 y + \beta_4 xy + \beta_5 y^2$	0.013	0.006	−0.038	−0.006	0.027	0.9814
B_z	$f(x,y) = \beta_1 + \beta_2 x + \beta_3 y$	0.078	0.038	0.079	–	–	0.1156

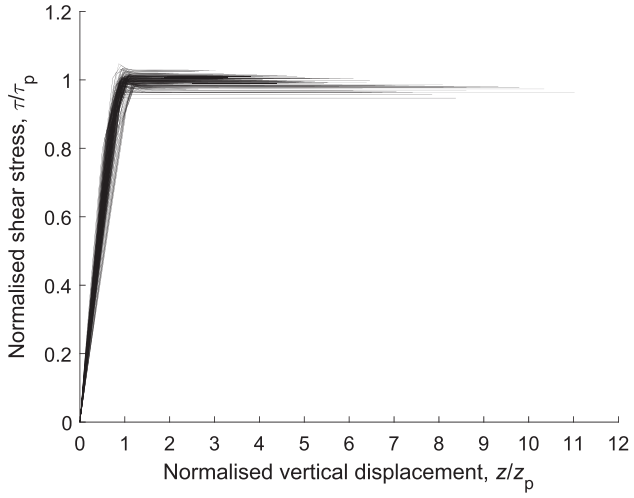

Fig. 11. Normalised t–z curves using the mathematical formulations of τ_p and z_p for predicting the frictional axial response during tensile loading in drained conditions. Results from all 25 related models are included.

the mathematical formulation of peak shear stress and the FE results (see Fig. 10(a)).

Upon normalising the results by implementing the mathematical models of τ_p and z_p, the curves related to all numerical models and depths align adequately (see Fig. 11). This serves as confirmation of two aspects: (*a*) the statistical model shows high fidelity with respect to original FE results; (*b*) the chosen *t–z* curve depicted in Fig. 9 is representative of frictional behaviour given drained conditions during tensile loading.

4.2. Undrained conditions

The formulation of peak shear stress undergoes in the same manner as in the drained case scenario, by adopting Eq. (9), followed by a study of parameters A_τ and B_τ, the results of which are summarised in Table 3. On the other hand, the peak displacement is estimated by using a slightly different approach than the one seen in Eq. (10):

$$\frac{z_p}{D} = A_z \left(\frac{\gamma' d}{\sigma_a \tan\phi} \right)^{B_z} \tag{11}$$

In Eq. (11) the peak displacement is normalised with the bucket diameter, while A_z and B_z are investigated as functions of only ϕ.

The notable difference introduced by the presence of excess pore pressure is the continuous increase of shear stress during post-failure. This behaviour is modelled by a straight line with positive slope, λ, as seen in Fig. 9. A significant spread of post-failure curves is evident in Fig. 12, which means that a single line with a constant slope reflects only the general tendency of shear stress development after failure and the modelling error becomes larger with displacements. Linear regression gives $\lambda = 0.0588$. The equation for *t–z* curves related to undrained conditions is written as

$$\frac{\tau}{\tau_p} = \begin{cases} \frac{z}{z_p} & \text{for } \frac{z}{z_p} < 1 \\ \lambda\left(\frac{z}{z_p} - 1\right) + 1 & \text{for } \frac{z}{z_p} \geq 1 \end{cases} \tag{12}$$

Table 3
Summary of β-coefficients used for modelling the undrained tensile response. Here x = D/D_{ref} and y = tanϕ.

Parameter	Fitting function	β_1	β_2	β_3	β_4	β_5	R^2
A_τ	$f(x,y) = \beta_1 + \beta_2 x + \beta_3 y$	−0.055	0.083	0.262	–	–	0.9712
B_τ	$f(x,y) = \beta_1 + \beta_2 x + \beta_3 y + \beta_4 x^2 + \beta_5 xy$	1.275	−0.770	−0.412	0.317	0.117	0.8369
A_z	$f(y) = \beta_1 + \beta_2 y$	0.00278	−0.00242	–	–	–	0.9837
B_z	$f(y) = \beta_1 + \beta_2 y$	1.675	−1.782	–	–	–	0.7298

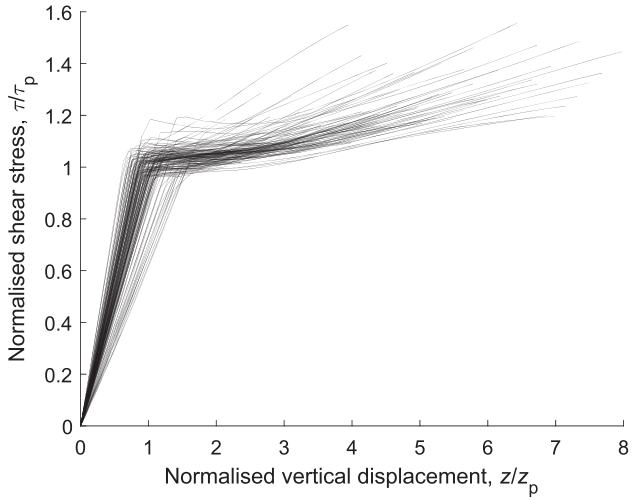

Fig. 12. Normalised t–z curves using the mathematical formulations of τ_p and z_p for predicting the frictional axial response during tensile loading in undrained conditions. Results from all 25 related models are included.

5. Formulation of *t–z* curves for compressive loading

The following considerations stemming from Fig. 8 constitute the basis for modelling the frictional response of buckets under compression.

- Due to large discrepancies between developments of skin friction along inner and outer skirt faces in drained conditions (see Fig. 8(a)), the two sides are treated individually, i.e. a distinct mathematical model is formulated for each side. Therefore, the total frictional response can be estimated in a two-step procedure: firstly, *t–z* curves for each side are generated separately, and then they are aggregated to obtain the total response. On the other hand, for compression under undrained conditions (see Fig. 8(b)), the *t–z* formulation follows the approach adopted in tension loading cases, where one mathematical model accounts for the total frictional response.
- Since failure occurs at the same displacement amplitudes at any depth within a numerical model, the vertical displacements may be normalised with respect to some constants, e.g. bucket diameter, *D*. The expressions for peak shear stress, τ_p, may be established by regression analysis according to the steps described earlier.
- Employing a single function, as opposed to a piecewise one, may suffice to accurately capture both pre- and post-failure responses, on grounds of relatively smooth transition between the two phases.

5.1. Drained conditions

5.1.1. Inner side

Comparing the shear stress development at various depths (see Fig. 8(a)), it is seen that the representative curves differ not only in magnitude, but also in shape and degree of non-linearity. It becomes clear that a full alignment of normalised curves can only be achieved around delimited parts thereof. For example, using the maximum reached shear stress as a normalising quantity yields adequate results in terms of aligning the curve tails, whereas significant divergence is present among other parts. In light of a necessary compromise, priority is attributed to accurate representation of initial displacements ($z/D < 0.01$). Applying Eq. (13) (API, 2000) to compute the ultimate skin friction, τ_u, leads to acceptable results regarding the normalisation of the initial response (see Fig. 13).

$$\tau_u = \sigma'_{v0} K_0 \tan\delta \tag{13}$$

The data from each model is fitted with a power function, thus the mathematical model adopts the following form

$$\frac{\tau}{\tau_u} = A(D,\phi)\left(\frac{z}{D}\right)^{B(D,\phi)} \tag{14}$$

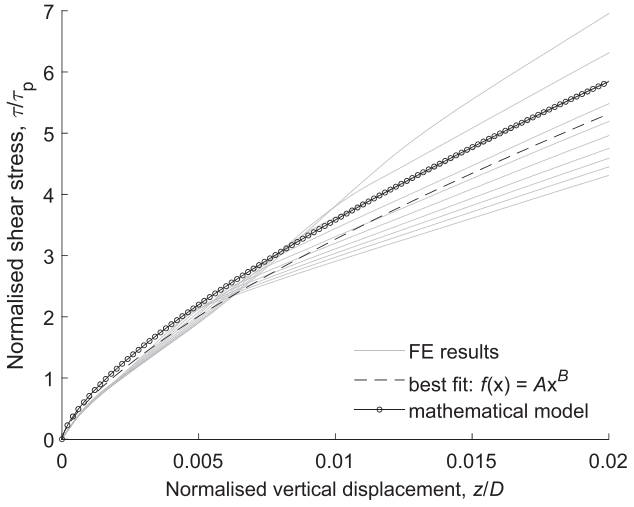

Fig. 13. Comparison between the normalised t–z curves at varied depths below mudline and the proposed mathematical model for estimating friction on the inner side of the skirt during drained compressive loading. The example relates to the numerical model where D = 15 m and ϕ = 35°.

Table 4
Summary of β-coefficients used for modelling the drained compressive response (inner side). Here x = D/D_{ref} and y = tanϕ.

Parameter	Fitting function	β_1	β_2	β_3	β_4	β_5	R^2
A	$f(x,y) = \beta_1 + \beta_2 x + \beta_3 y + \beta_4 x^2 + \beta_5 xy$	−522.5	156.1	1069.6	92.8	−547.1	0.9786
B		−0.200	0.437	1.362	0.093	−0.824	0.9654

where parameters *A* and *B* are studied as functions of bucket diameter and friction angle. The details of the study in question are given in Table 4.

5.1.2. Outer side

Eq. (9) is used for estimating the peak shear stress. Table 5 displays the corresponding *β*-coefficients.

A function composed of a hyperbolic tangent and a proportional term represents an acceptable candidate for fitting the normalised *t–z* curves. The mathematical model is expressed as follows

$$\frac{\tau}{\tau_p} = C_1 \tanh\left(C_2(\phi)\frac{z}{D}\right) + C_3(\phi)\frac{z}{D} \tag{15}$$

Regression analysis of *C*-coefficients yields sets of 25 values for each of them. Significant correlation with friction angle is found for C_2 and C_3, while the mean value $C_1 = 1.032$ is used for the first coefficient.

$$C_2 = 2631.5\tan\phi - 889.4$$

$$C_3 = 213.6\tan\phi - 115.2$$

The best fit curves and the proposed *t–z* curves are illustrated in Fig. 14.

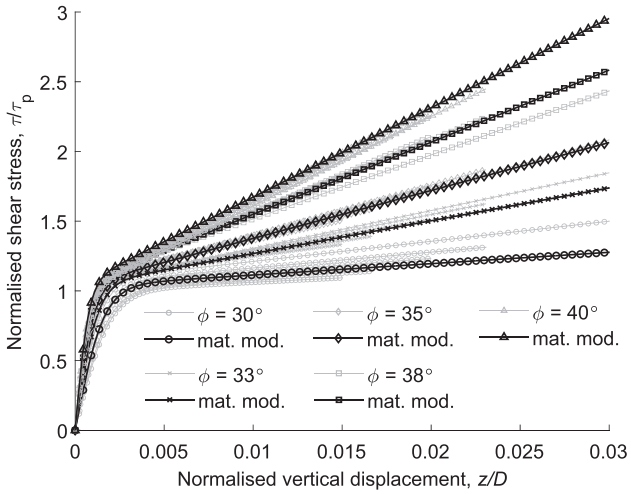

Fig. 14. Comparison between the best fit curves (in grey) from all numerical models and the proposed mathematical model curves for estimating friction on the outer side of the skirt during drained compressive loading.

5.2. Undrained conditions

Eq. (15) may be used to predict the frictional response given undrained conditions, especially since it can account for a shear stress decrease during post-failure. Moreover, the dependency of *C*-coefficients on both *D* and *ϕ* is considered for the current drainage conditions. The peak shear stress can be approximated with the power function given by Eq. (9). Table 6 presents the results of the parametric study of coefficients.

The flexibility of the proposed *t–z* curves is evident in Fig. 15, as both the growth and decay in skin friction are captured.

6. Illustrative comparison study

The load–displacement curves constructed with the proposed *t–z* curves are in close agreement with the ones extracted directly from the numerical models (see Fig. 16). The latter represent aggregates of results from interface stress points along entire skirt lengths, including the extremities (the ones that were discarded in the process of formulating the *t–z* models). Deviations between the two sets of curves increase with displacements. The errors stem from inaccuracies associated with regression analysis and with the assumption that shear stress development exhibits identical trends at all points along the skirt face. This assumption has larger consequences for modelling undrained behaviour, since hydraulic gradients influence soil–structure interaction at skirt edges to a significant degree. The curves recommended by API (2000) yield conservative results for ultimate skin friction and predict earlier displacement at which it is reached.

Fig. 17 shows comparison plots between the load–displacement curves generated with the proposed *t–z* model and results from three numerical studies. All three of them investigated suction buckets subjected to tensile loads. Achmus & Thieken (2014) and Thieken et al. (2014) implemented an advanced hypoplastic soil model and validated it with experimental results obtained by Iskander et al.

Table 5
Summary of β-coefficients used for modelling the drained compressive response (outer side). Here x = D/D_{ref} and y = tanϕ.

Parameter	Fitting function	β_1	β_2	β_3	R^2
A_τ	$f(x,y) = \beta_1 + \beta_2 x + \beta_3 y$	−0.170	0.150	0.334	0.9808
B_τ		0.595	0.085	−0.534	0.8987

Table 6
Summary of β-coefficients used for modelling the undrained compressive response. Here x = D/D_{ref} and y = tanϕ.

Parameter	Fitting function	β_1	β_2	β_3	β_4	β_5	β_6	R^2
A_τ	$f(x,y) = \beta_1 + \beta_2 x + \beta_3 y$	−0.205	0.121	0.435	–	–	–	0.9811
B_τ		0.239	0.077	0.185	–	–	–	0.7436
C_1	$f(x,y) = \beta_1 + \beta_2 x + \beta_3 y + \beta_4 x^2 + \beta_5 xy + \beta_6 y^2$	0.277	−0.063	2.519	−0.255	0.761	−2.252	0.7589
C_2	$f(x,y) = \beta_1 + \beta_2 x + \beta_3 y + \beta_4 xy + \beta_5 y^2$	−3329.1	−352.8	10872.9	473.2	−6674.6	–	0.9352
C_3	$f(x,y) = \beta_1 + \beta_2 x + \beta_3 y$	−116.2	28.4	146.2	–	–	–	0.9834

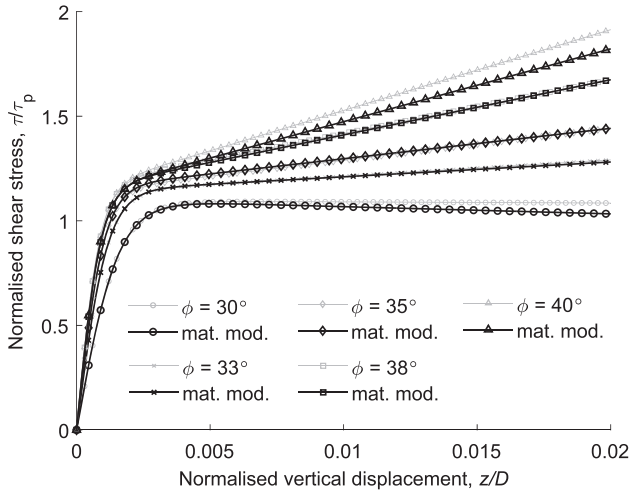

Fig. 15. Comparison between the best fit curves (in grey) from five numerical models (D = 15 m) and the proposed mathematical model curves for estimating skirt friction during undrained compressive loading.

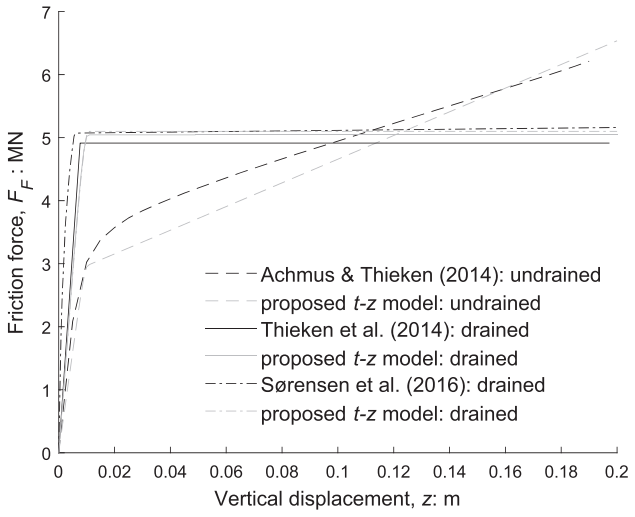

Fig. 17. Load–displacement curves computed with the proposed t–z formulation and compared with other numerical studies using equivalent bucket dimensions and soil properties.

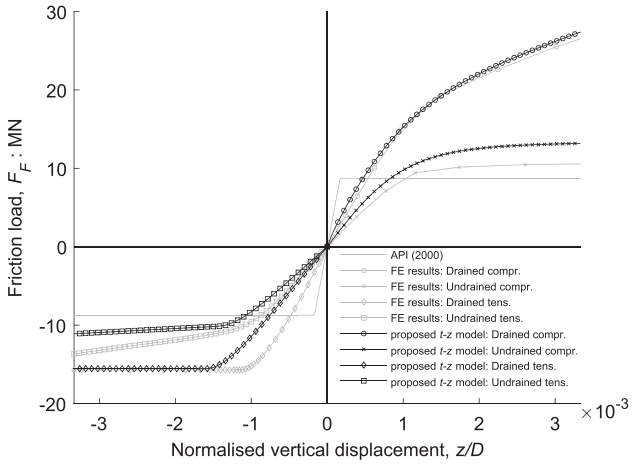

Fig. 16. Load–displacement curves given all four combinations between loading and drainage conditions. The example relates to the numerical model where D = 15 m and ϕ = 35°.

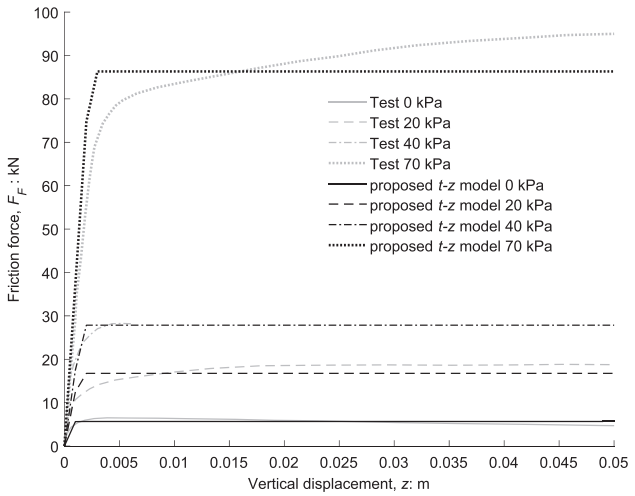

Fig. 18. Comparison between load–displacement curves from medium-scale physical tests (Vaitkunaite, 2016) and the ones computed with the proposed t–z formulation.

(1993). The Mohr-Coulomb constitutive model was used by Sørensen et al. (2016). Reasonable agreement is found with all studies.

Vaitkunaite (2016) tested a suction bucket model (D = 1 m, L = 0.5 m) installed in a cylindrical container of 2.5 m in diameter and 1.5 m in height. The container was filled with dense sand ($D_r \approx 81\%$) and the model was subjected to monotonic drained tensile loading. Various levels of overburden pressure were applied over the soil surface to simulate various depths. In Fig. 18, every curve representing experimental results is linked to the respective magnitude of applied overburden pressure. The *t–z* formulation can accurately predict the stiffness and capacity, as

well as the displacement at which the peak stress is reached. However, it does not capture the hyperbolic trend of stiffness degradation, at least given the current set of input parameter values.

It is emphasised that the mathematical models may prove highly inaccurate or become unstable if very small foundation dimensions or friction angles are used. Since the formulation of *t–z* curves is based on statistical analysis of data from numerical models of buckets with diameter and skirt lengths between 10 and 20 m and friction angles between 30° and 40°, any extrapolation beyond the range of investigated values may lead to unexpected results.

7. Conclusions

A set of four *t–z* curves for suction buckets are formulated in this paper. These curves describe the behaviour of non-linear axial springs that represent friction between bucket skirt and soil. Each formulation relates to a specific case that involves a combination of loading direction (tension or compression) and drainage condition (drained or undrained). The proposed relationships are based on regression analysis of results from 100 finite-element models of suction buckets installed in a typical marine sand. The results of the current research match the ones of other numerical studies to a high degree. In addition, the proposed *t–z* model is successfully validated with experimental results.

The static *t–z* curves may be conveniently implemented at the preliminary stages of foundation design, since they require three basic variables as input parameters: bucket diameter, sand's friction angle and initial vertical overburden pressure. Thus, a minimum amount of site-specific data is sufficient for enabling the use of proposed mathematical models. It is emphasized that the current formulation relates only to skirt friction, therefore the global vertical response can be assessed only in case of drained tensile loading. Load–displacement curves derived with the proposed *t–z* formulation cover a part of what practising engineers may require to obtain initial estimates of minimum bucket dimensions with respect to fulfilling ULS and SLS conditions. For analysing the total axial response under compression or undrained tension loading, other contributing factors must be considered, such as differential water pressure under the bucket lid and soil reaction under the bucket lid and skirt toe.

It is also important to consider that the proposed formulation is based on pure vertical loading. Horizontal loading and bending moments were not included in the FE analyses. The impact of these forces on suction buckets within a jacket structure is subject to further research.

Modelling geostructures by discretising the system into springs has found decades-long success within pile design, therefore the presented work does not bring novelty at the conceptual level. Rather, it is the new context of bucket foundations that highlights its uniqueness.

Acknowledgements

The authors gratefully acknowledge the financial support received from the European Union through the Horizon 2020 research programme. This study is funded as part of i4Offshore project (Integrated Implementation of Industrial Innovations for Offshore Wind Cost Reduction) under grant agreement no. 818153.

References

Achmus, M., Kuo, Y.-S., Abdel-Rahman, K., 2009. Behavior of monopile foundations under cyclic lateral load. Comput. Geotech. 36, 725–735.

Achmus, M., Akdag, C.T., Thieken, K., 2013. Load-bearing behaviour of suction bucket foundations in sand. Appl. Ocean Res. 43, 157–165.

Achmus, M., Thieken, K., 2014. Numerical simulation of the tensile resistance of suction buckets in sand. J. Ocean Wind Energ. 1 (4), 231–239.

Achmus, M., Gütz, P., 2016. Numerical modeling of the behavior of bucket foundations in sand under cyclic tensile loading. In: Zingoni, A. (Ed.), Proceedings of the 6th International Conference on Structural Engineering, Mechanics and Computation. Leiden, The Netherlands: CRC Press/Balkema, pp. 2085–2091.

API (American Petroleum Institute), 2000. Recommended practice for planning, designing, and constructing fixed offshore platforms—working stress design, RP 2A-WSD, 21st ed., Washington, DC, USA: American Petroleum Institute.

Barari, A., Ibsen, L.B., 2012. Undrained response of bucket foundations to moment loading. Appl. Ocean Res. 36, 12–21.

Barari, A., Bagheri, M., Rouainia, M., Ibsen, L.B., 2017. Deformation mechanisms for offshore monopile foundations accounting for cyclic mobility effects. Soil Dynam. Earthquake Engng 97, 439–453.

Barari, A., Ibsen, L.B., 2018. A macro-element approach for non-linear response of offshore skirted footings. In: Khabbaz, H., Youn, H., Bouassida, M. (Eds.), New Prospects in Geotechnical Engineering Aspects of Civil Infrastructures. GeoChina 2018. Sustainable Civil Infrastructures. Cham, Switzerland: Springer, pp. 127–139.

Biot, M.A., 1962. The mechanics of deformation and acoustic propagation in porous media. J. Appl. Phys. 33, 1482–1498.

Bohn, C., dos Santos, A. L., Frank, R., 2016. Development of axial pile load transfer curves based on instrumented load tests. J. Geotech. Geoenviron. Engng. 143(1), Paper No. 04016081.

Bolton, M.D., 1986. The strength and dilatancy of sands. Géotechnique 36 (1), 65–78. https://doi.org/10.1680/geot.1986.36.1.65.

Chan, A.H.-C., 1988. A unified finite element solution to static and dynamic problems of geomechanics PhD thesis. University College of Swansea, Swansea, UK.

Coyle, H.M., Sulaiman, I.H., 1967. Skin friction for steel piles in sand. J. Soil Mech. Found. Div. Am. Soc. Civ. Engrs. 93 (6), 261–278.

Deng, W., Carter, J.P., 2002. A theoretical study of the vertical uplift capacity of suction caissons. Int. J. Offshore Polar Engng 12 (2), 89–97.

DNV (Det Norske Veritas), 1992. Foundations. Classification Notes No. 30.4. Oslo, Norway: Det Norske Veritas.

Fleming, W.G.K., 1992. A new method for single pile settlement prediction and analysis. Géotechnique 42 (3), 411–425. https://doi.org/10.1680/geot.1992.42.3.411.

Hardin, B.O., Black, W.L., 1969. Closure to "Vibration modulus of normally consolidated clay". J. Soil Mech. Found. Div. Am. Soc. Civ. Engrs. 95 (6), 1531–1537.

Hardin, B.O., Drnevich, V.P., 1972. Shear modulus and damping in soils: design equations and curves. J. Soil Mech. Found. Div. Am. Soc. Civ. Engrs. 98 (7), 667–692.

Hossain, M.S., Randolph, M.F., 2009. New mechanism-based design approach for spudcan foundations on single layer clay. J. Geotech. Geoenviron. Engng 135 (9), 1264–1274.

Ibsen, L. B., Larsen, K. A., Barari, A., 2014. Calibration of failure criteria for bucket foundations on drained sand under general loading. J. Geotech. Geoenviron. Engng 140(7), Paper No. 04014033.

Iskander, M. G., Olson, R. E., Pavlicek, R. W., 1993. Behavior of suction piles in sand. In: Nelson, P.P., Smith, T.D., Clukey, E.C. (Eds.), Design and performance of deep foundations: piles and piers in soil and soft rock. New York, NY, USA: American Society of Civil Engineers, pp. 157–171.

Janbu, N., 1967. Settlement calculations based on the tangent modulus concept. Three guest lectures at Moscow State University. Bulletin No. 2, Norwegian Institute of Technology, Trondheim, Norway.

Kraft Jr., L.M., Ray, R.P., Kagawa, T., 1981. Theoretical t–z curves. J. Geotech. Engng Div. Am. Soc. Civ. Engrs. 107 (11), 1543–1561.

Larsen, K.A., Ibsen, L.B., Barari, A., 2013. Modified expression for the failure criterion of bucket foundations subjected to combined loading. Can. Geotech. J. 50 (12), 1250–1259.

Lombardi, D., Dash, S.R., Bhattacharya, S., Ibraim, E., Muir Wood, D., Taylor, C.A., 2017. Construction of simplified design *p–y* curves for liquefied soils. Géotechnique 67 (3), 216–227. https://doi.org/10.1680/jgeot.15.P.116.

Lu, Q., Luo, Q., 2018. A load transfer approach for studying the load–deformation response of vertically loaded single pile. In: Chen, R., Zheng, G., Ou, C. (Eds.), Proceedings of the 2nd international symposium on Asia Urban Geo Engineering, pp. 369–384. Singapore: Springer.

Mana, D.S.K., Gourvenec, S., Randolph, M.F., Hossain, M.S., 2012. Failure mechanisms of skirted foundations in uplift and compression. Int. J. Phys. Model. Geotech. 12 (2), 47–62.

Mana, D.S.K., Gourvenec, S., Randolph, M.F., 2014. Numerical modelling of seepage beneath skirted foundations subjected to vertical uplift. Comput. Geotech. 55, 150–157.

Nanda, S., Patra, N.R., 2014. Theoretical load-transfer curves along piles considering soil nonlinearity. J. Geotech. Geoenviron. Engng 140 (1), 91–101.

Nielsen, S. K., Shajarati, A., Sørensen, K. W., Ibsen, L. B., 2012. Behaviour of dense Frederikshavn sand during cyclic loading. DCE Technical Memorandum No. 15. Department of Civil Engineering, Aalborg University, Aalborg, Denmark.

Oh, K.-Y., Nam, W., Ryu, M.S., Kim, J.-Y., Epureanu, B.I., 2018. A review of foundations of offshore energy convertors: current status and future perspectives. Renew. Sust. Energ. Rev. 88, 16–36.

Østergaard, M. U., Knudsen, B. S., Ibsen, L. B., 2015. P-y curves for bucket foundations in sand using finite element modeling. In: Meyer, V. (Ed.), Frontiers in Offshore Geotechnics III: Proceedings of the 3rd international symposium on frontiers in offshore geotechnics, vol. 1, pp. 343–348. London, UK: CRC Press.

Park, J.-S., Park, D., Yoo, J.-K., 2016. Vertical bearing capacity of bucket foundations in sand. Ocean Engng. 121, 453–461.

Park, J.-S., Park, D., 2017. Vertical bearing capacity of bucket foundation in sand overlying clay. Ocean Engng. 134, 62–76.

Plaxis, 2017. PLAXIS 2D Manuals. Delft, The Netherlands: Plaxis bv.

Randolph, M.F., Wroth, C.P., 1978. Analysis of deformation of vertically loaded piles. J. Geotech. Engng Div. Am. Soc. Civ. Engrs. 104 (12), 1465–1488.

Schanz, T., Vermeer, P.A., Bonnier, P.G., 1999. The hardening soil model: formulation and verification. In: Brinkgreve, R.B.J. (Ed.), Beyond 2000 in computational geotechnics. Balkema, Rotterdam, The Netherlands.

Seed, H.B., Reese, C., 1957. The action of soft clay along friction piles. Trans. Am. Soc. Civ. Engrs. 122 (1), 731–754.

Shen, K., Zhang, Y., Klinkvort, R. T., Sturm, H., Jostad, H. P., Sivasithamparam, N., Guo, Z., 2017. Numerical simulation of suction bucket under vertical tension loading. Proceedings of the 8th international conference on offshore site investigation and geotechnics, London, UK, vol. 1, pp. 488–497.

Sjelmo, Å., 2012. Soil–structure interaction in cohesionless soils due to monotonic loading MSc thesis. Aalborg University, Aalborg, Denmark.

Skau, K.S., Jostad, H.P., Eiksund, G., Sturm, H., 2019. Modelling of soil–structure–interaction for flexible caissons for offshore wind turbines. Ocean Engng. 171, 273–285.

Sørensen, E.S., Clausen, J., Damkilde, L., 2016. Comparison of numerical formulations for the modeling of tensile loaded suction buckets. Comput. Geotech. 83, 198–208.

Sturm, H., 2017. Design aspects of suction caissons for offshore wind turbine foundations. Proceedings of TC 209 workshop at the 19th International Conference on Soil Mechanics and Geotechnical Engineering, Seoul, South Korea, pp. 45–63.

Thieken, K., Achmus, M., Schröder, C., 2014. On the behavior of suction buckets in sand under tensile loads. Comput. Geotech. 60, 88–100.

Tjelta, T. I., 2015. The suction foundation technology. In: Meyer, V. (Ed.), Frontiers in Offshore Geotechnics III: Proceedings of the 3rd International Symposium on Frontiers in Offshore Geotechnics, vol. 1, pp. 85–94. London, UK: CRC Press.

Vahdatirad, M. J., Troya Diaz, A., Nielsen, S., Ibsen, L. B., Andersen, L. V., Firouzianbandpey, S., Griffiths, D. V., 2016. A load-displacement based approach to assess the bearing capacity and deformations of mono-bucket foundations. In: Zingoni, A. (Ed.), Proceedings of the 6th International Conference on Structural Engineering, Mechanics and Computation. Leiden, The Netherlands: CRC Press/Balkema, pp. 2105–2111.

Vaitkunaite, E., 2016. Physical modelling of bucket foundations subjected to axial loading PhD thesis. Aalborg University, Aalborg, Denmark.

Vaitkunaite, E., Nielsen, B.N., Ibsen, L.B., 2016. Bucket foundation response under various displacement rates. Int. J. Offshore Polar Engng 26 (2), 116–124.

Vijayvergiya, V. N., 1977. Load–movement characteristics of piles. Proceedings of the 4th annual symposium of the Waterway, Port, Coastal, and Ocean Division of ASCE, Los Angeles, CA, USA, vol. 2, pp. 269–284.

Wang, Z., Xie, X., Wang, J., 2012. A new nonlinear method for vertical settlement prediction of a single pile and pile groups in layered soils. Comput. Geotech. 45, 118–126.

Wang, X., Zeng, X., Li, J., Yang, X., Wang, H., 2018. A review on recent advancements of substructures for offshore wind turbines. Energ. Convers. Manage. 158, 103–119.

Winkler, E., 1867. Die Lehre von der Elasticitaet und Festigkeit. Prague: Dominicus, (in German).

Wolf, T. K., Rasmussen, K. L., Hansen, M., Roesen, H. R., Ibsen, L. B., 2013. Assessment of p–y curves from numerical methods for a non-slender monopile in cohesionless soil. DCE Technical Memorandum No. 64. Department of Civil Engineering, Aalborg University, Aalborg, Denmark.

Zafeirakos, A., Gerolymos, N., 2016. Bearing strength surface for bridge caisson foundations in frictional soil under combined loading. Acta Geotech. 11 (5), 1189–1208.

Zhou, W., Guo, Z., Wang, L., Rui, S., 2019. Dynamic responses of jacket foundation offshore wind turbine considering the cyclic loading effects. In Ferrari, A., Laloui, L. (Eds.), Energy Geotechnics, SEG 2018, pp. 451–458. Cham, Switzerland: Springer.

Zienkiewicz, O. C., Chan, A. H.-C., Pastor, M., Paul, D. K., Shiomi, T., 1990. Static and dynamic behaviour of soils: a rational approach to quantitative solutions. I. Fully saturated problems. Proc. Royal Soc. London. A. Math. Phys. Sci. 429, 285–309.